Biomechan Model Mechanobiol (2006) 5: 39–52
DOI 10.1007/s10237-005-0009-7

ORIGINAL PAPER

Thibault Lemaire · Salah Naïli · Agnès Rémond

Multiscale analysis of the coupled effects governing the movement of interstitial fluid in cortical bone

Received date: 19 July 2005 / Accepted date: 25 October 2005 / Published online: 20 December 2005

Abstract A multiscale approach (periodic homogenization) is carried out to model osteon's behaviour, and especially the coupled phenomena that govern its interstitial fluid movement. Actions of electro-osmotic and osmotic motions in addition to the classical Poiseuille flow are studied at the mesoscale of the canaliculus and within the micropores of the collagen-apatite matrix. Use of this fully coupled modelling leads to a comparison of these different effects. Limitation of a classical Darcian description of the fluid flow at the two scales is so studied. For each of these studies a special attention is given to the pore's geometry influence and to their electrical and hydraulic properties.

1 Introduction

Cortical bone is a saturated porous tissue composed of a solid matrix, cells and a fluid phase. Its behaviour is governed by different effects due to many driving forces, such as hydraulic, chemical, electrical and mechanical. The movement of the fluid phase within the pores or spaces of the solid matrix is referred to as interstitial fluid flow. Although much is suspected on the role of fluid movement on cell behaviour, relatively little is known about the characteristics of pores through which fluid flows or about the flow characteristics under in vivo conditions. Despite this lack of information on interstitial fluid movement in bone, its role in physiological processes like adaptation and repair mechanisms has been recognized to be essential in the literature (Cowin 2002). The difficulty to understand interstitial fluid biological effects is due to different causes. Indeed, it is quite difficult to carry out measurements to describe phenomena governing bone's response to a given stimulus. Moreover different existing models, which need experimental data to be realistic, require to make significant simplifications to represent such living materials behaviour. To illustrate this complexity, if electric phenomena have been observed in the bone since the fifties (Yasuda 1964; Basset and Becker 1962), their physiological origin is still debated (Pollack 2001).

Furthermore, an important property inherent to the one's pores walls is the negative charge present on their surface. The resulting electric potential is compensated by the adsorption of cations on the surface forming the inner compact layer commonly referred to as the immobile Stern layer. Nevertheless, most of the cations are located in the electrolyte aqueous solution. They form a diffuse layer made of mobile charges. In general, the equilibrium structure of completely dissociated electrolytes next to the walls is modelled by classical electrostatics equations, where charge distribution and electrical field are governed by a Poisson–Boltzmann equation (Israelachvili 1991). When advected by the streaming velocity of the fluid, the excess in mobile charge population in the counter-ion atmosphere leads to macroscopically observed electrokinetic phenomena, such as streaming currents. To conserve charge, the movement of the net charge generates an electric potential, often referred to as streaming potential, which may give rise to other macroscopically electrokinetic phenomena. Spatial variations of this streaming potential can also force mobile charges to move, causing an electro-osmotic seepage because of the viscous drag interaction between ions and water (Hunter 1981). In addition to theses electrokinetic phenomena, a flow driven by chemical-osmotic effects can also occur when the salinity varies spatially (Gu et al. 1998).

In addition to these electro-chemical phenomena other factors, such as hormonal action or exercices, can have an effect on the interstitial fluid flow. The present model does not consider explicitly all these related factors. This study is mainly focused on hydro-electro-chemical couplings. Nevertheless, some of these factors are implicitly studied here. For

T. Lemaire · Salah Naïli (✉) · A. Rémond
Laboratoire de Mécanique Physique,
CNRS UMR 7052 B2OA Faculté des Sciences et Technologie,
Université Paris XII-Val de Marne 61, Avenue du Général de Gaulle,
94010 Créteil Cédex, France
E-mail: lemaire@univ-paris12.fr
E-mail: naili@univ-paris12.fr
E-mail: a.remond@univ-paris12.fr
Tel.: +33-1-45171445
Fax: +33-1-45171433

instance, ageing influences geometry and chemical properties of bone tissues. Variations of these two parameters are taken into account in our study.

Classical mechanical descriptions of cortical bone use poroelasticity theory (Pollack et al. 1984; Cowin et al. 1995; Mak and Zhang 2001; Rémond and Naili 2004; Gururaja et al. 2005) deriving from Biot's works (Biot 1941). Electro-chemical effects are not always accounted for in these models. Some authors, using a zero charge flux assumption, are able to identify the streaming current with the fluid flow evaluated from a Darcy's law or Brinkman's equation (Cowin 2001). Doing this, the generated streaming potential is only seen as a consequence of the flow, whereas it also acts as a driving force on the fluid movement.

The aim of this work is to clarify the role of electro-chemical couplings in the interstitial fluid movement. Cortical bone is a multi-scaled medium where multi-physical phenomena can occur. Since the key elements of couplings are located at the pore scale, the strategy proposed in the present work is to obtain the fluid movement by upscaling the local description. Periodic homogenization is the technique used to propagate physical informations to the upper scale. As exposed in the following section, cortical medium can be characterized by three levels of porosity. Cowin (2001) suggested that the porosity that may play a significant role in the mechanotransduction processes is either the lacuno-canalicular porosity or the micropores of the collagen-apatite matrix. At these two scales the solute movement can be described by coupling the Stokes and Poisson–Boltzmann equations. Thus, a comparison between hydraulic, electro-osmotic and osmotic contributions to the total fluid transport is proposed and compared at each structural level.

In summary, in the present work, the solid matrix of the cortical bone is assumed to be characterized by a porous medium regularly structured with three levels of porosity. Each level of porosity is supposed to be spatially uniform. The interstitial fluid is represented by a saline solution. It is accepted that the movement of this fluid is only due to hydraulic, chemical, electrical and mechanical driving forces. Moreover, the movement of this fluid is only studied in the extravascular spaces of the canaliculi and micropores inside the solid matrix.

After this introduction on the rationale for studying coupled phenomena in bone fluid flow, geometry and fluid descriptions are given in Sects. 2 and 3. The changes of variables used in the homogenization method are then described in Sect. 4. Section 5 deals with the upscaling procedure of the homogenization method. Solutions for fluid flow at each scale are given in Sect. 6. Results and their implications on coupling phenomena occurring in bone fluid flow are discussed in Sect. 7. Finally, a conclusion is drawn in Sect. 8.

2 Geometrical configuration and levels of porosity

Cortical bone tissue presents a well organized structure composed of mineralized cylinders called osteons. These osteons, which present diameters of a few hundreds of micrometers, are centered on Haversian canals (Fig. 1). These osteonal canals and other large transverse pathways in the bone matrix (Volkmann canals) contain the vasculature, the nerves and interstitial fluid. In addition to those channels, other smaller pathways exist through which fluid can flow. The aim of this section is to describe this multi-scale organization and in particular to model geometry of different interstitial flow pathways. Mineral composition and microstructure of the osteon are supposed to be spatially uniform.

Spaces within bone have size that can vary from visible cavities to very small pores. Their sizes stretch over several orders of magnitude. At each of these spatial scales, pore sizes correlate with different structural components. As bone permeability is highly dependent on this microstructure, measurements of this parameter often cover a large range of values (Arramon and Nauman 2001).

Three main levels of porosity inside bone are commonly distinguished. From the largest to the smallest, there are the vascular spaces (Haversian and Volkmann canals), the spaces associated with the lacuno-canalicular system and the collagen-apatite matrix pores. In the present work, the scale for each level of porosity is respectively referred to as the macroscale (osteon's transversal size, Fig. 1a), the mesoscale (canaliculus transversal size, Fig. 1b) and the microscale (collagen-apatite matrix pores transversal size, Fig. 1c).

In cortical bone, the pathways of transport from the blood supply to the osteocytes are due, on one hand, to the vessels of the vascular system and, on the other hand, to the extravascular fluid spaces comprising the lacuno-canalicular system and the collagen-apatite matrix pores. The function of Haversian capillaries might be to alternatively serve as either pathways for nutrient transport or as drainage canals, regulated by vasomotor function of the sphincter at the arterial end. Thus, the interstitial fluid may flow faster in one region and slower in another. In the present study, the attention is only focused on the fluid movement in the extravascular pores. As a consequence, variations of the flow in the vascular macropores are not considered and can only interfere through the boundary conditions in term of pressure or velocity variations.

Concerning the canaliculus, it can be considered as a capillary (with circular cross-section) whose diameter of a few hundreds of nanometers is noted as $2R_C$. The osteocyte cell process is located along the canaliculus axis. It can be seen as a cylinder whose circular cross-section has a radius R_M around 50 nm. Moreover, geometrical perturbation introduced by the presence of the lacunae is not taken into account. Micropores of the collagen-apatite matrix are not yet well known. They correspond to spaces between collagen and crystallites of the mineral apatite. The characteristic size R_m of micropores has been measured by Holmes et al. (1953) and it varies between 5 and 12.5 nm. In the present model, micropores are assumed to be cylinders with circular cross-section. As a consequence, equations developed in the present model at the mesoscale and at the microscale can be treated with cylindrical coordinates. No matter which scale is considered, the fluid flow develops in the longitudinal direction

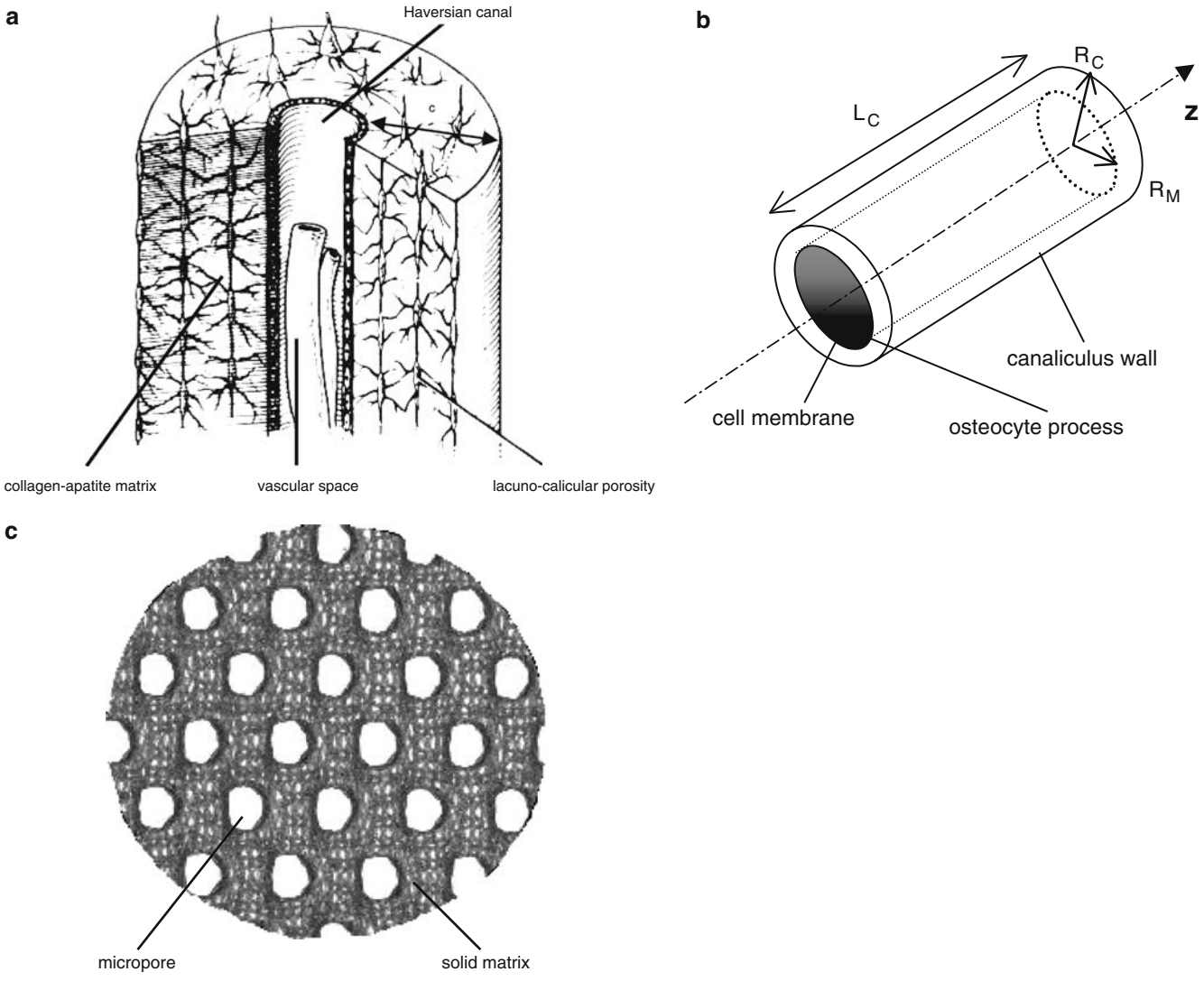

Fig. 1 Schematic representation of an osteon: the three levels of porosity. **a** Macroscale of the osteon; **b** Mesoscale of the canaliculus; **c** Microscale of the pores in the collagen-apatite matrix (adapted from Buckwalter et al. (1995))

of the pore (coordinate z) whereas its local fields (electric potential, ionic concentrations, velocity ...) may also vary in the radial direction (coordinate r). For that reason, equations are formally similar at both scales (mesoscale and microscale) but the boundary conditions are not, and problems at the canaliculus scale and in the micropores are independently treated. Although notations of the coordinates at each scale are the same, they describe coordinates for each given scale.

3 Description of the fluid

The aim here is to describe locally the fluid. Its material properties are identical at any level of porosity. We consider that pores are saturated by an aqueous solution consisting of water and an entirely dissociated salt with monovalent electrolytes (typically sodium and calcium ions). For simplicity we neglect steric and hydration effects assuming the liquid phase as structureless dielectric electrolyte solution with ions treated as point charges.

3.1 Electrostatics

When effects of the magnetic field are neglected, Maxwell's equations reduce to the Poisson equation (Hunter 2001):

$$\Delta\phi = -\frac{F}{\varepsilon\varepsilon_0}(n^+ - n^-), \tag{1}$$

where ϕ is the electric potential in the fluid phase, n^+ and n^- the cationic and anionic concentrations, respectively, ε_0 the vacuum permittivity, ε the relative dielectric constant of the solvent, F the Faraday constant and Δ the Laplace's operator.

In the canaliculus, boundary conditions are obtained by imposing the electric potential continuity on its wall and on the osteocyte process surface. In the collagen-apatite matrix,

these boundary conditions result from the electric potential continuity on the wall and the assumed axisymmetric property of pores.

The different surface potentials (walls of the calcified matrix and cell membrane) do not have the same origins. If the negative surface charge of the cell membrane is due to the presence of fatty acids, charge deficiency of the calcified matrix might result from different phenomena. That is why surface potentials are a priori different from one surface to the other. Moreover, estimation of the information associated with the electrical effects is difficult to obtain. For this reason, the zeta potential, potential at the slip line separating adsorbed ions from diffuse ones, gives a good estimate of the surface's electrical potential. Measurements of zeta potentials within bone vary because of different experimental conditions. Thus, Berreta and Pollack (1986) proposed a value of -3.55 mV whereas Kim et al. (2002) measured zeta potentials of -20 mV. Influence of these dispersions on phenomena described in the present work will be studied.

3.2 Movement of the electrolyte solution

The electrolyte solution is assumed to be incompressible and Newtonian. Its movement is governed by electrohydrodynamics. Neglecting gravity, convective and inertial effects, the Stokes flow is given by (Landau and Lifshitz 1960):

$$\mu_f \Delta \mathbf{v} - \nabla p = -F(n^+ - n^-)\mathbf{E}, \tag{2}$$

where $\mathbf{v}$ is the fluid velocity, p the hydraulic pressure, $\mathbf{E}$ the electrical field, μ_f the fluid dynamic viscosity and ∇ the gradient operator. Moreover fluid mass conservation is given by:

$$\nabla \cdot \mathbf{v} = 0, \tag{3}$$

where the divergence operator is noted $\nabla\cdot$. Corresponding boundary conditions are provided by the assumption that the fluid adheres to the wall.

3.3 Ions transport

Ionic concentrations are assumed to be small enough to neglect interactions between ions so that diffusion can be described by a double binary diffusion cations/water and anions/water. Ion movement is due to three contributions: (1) Brownian diffusion characterized by diffusion coefficients in water D_+ and D_- for cations and anions; (2) convective transport with the solvent; (3) and electromigration resulting from the electric field. Thus, the two ionic transport equations are written as follows:

$$\frac{\partial n^\pm}{\partial t} + \nabla \cdot (n^\pm \mathbf{v}) = \nabla \cdot \left(\frac{D_\pm n^\pm}{RT} \nabla \mu^\pm \right), \tag{4}$$

where $\mu^\pm$ are the electrochemical potentials of cations and anions, T is the absolute temperature (constant in vivo condition) and R the gas constant of ideal gas. Accepting the infinitely diluted solution assumption (Lyklema 1995), the electrochemical potentials can be expressed by:

$$\mu^\pm = \pm F\phi + RT \ln(n^\pm) + f(T, p), \tag{5}$$

where ln is the natural logarithm function.

The function f a priori depends on the pressure, but it is often accepted to change slowly with this parameter. Combining Eqs. (4) and (5), the Nernst–Planck equation is obtained (Samson et al. 1999):

$$\begin{aligned} &\frac{\partial n^\pm}{\partial t} + \nabla \cdot (n^\pm \mathbf{v}) = \nabla \cdot (D_\pm (\nabla n^\pm \pm n^\pm \nabla \bar{\phi})) \\ &\quad = \nabla \cdot (D_\pm \exp(\pm\bar{\phi} \nabla (n^\pm \exp(\pm\bar{\phi})))), \end{aligned} \tag{6}$$

where the reduced electric potential $\bar{\phi} = F\phi/RT$ is introduced.

4 Change of variables in the fluid

An innovative approach of this paper consists in the use of a change of variable in the fluid based on the fictive solution concept. Such an approach is sometimes used to describe coupled transport in electrically charged porous media and has been used with success, for instance, in clay modelling (Dormieux et al. 1995; Moyne and Murad 2002a; Lemaire et al. 2002; Lemaire 2004). Expressing the problem in terms of new fictive variables, it will be possible to distinguish between variables, called fast and slow variables for the microscale and macroscale, respectively, through an upscaling procedure. Theses variables might vary at the pore scale.

4.1 Notion of equivalent bulks

At a given point, the fluid corresponds to an equivalent bulk. It is a virtual solution verifying electroneutrality. Thus, we can write for each point occupied by the fluid phase:

$$n_b^+ = n_b^- = n_b, \tag{7}$$

where n_b^+ and n_b^- are the bulk concentrations respectively of the cations and the anions.

As proposed by the approach of Sasidhar and Ruckenstein (1981), the streaming potential, which is the electric potential that develops in order to maintain electroneutrality, corresponds to the electric potential inherent to the species of a bulk solution locally constructed at thermodynamic equilibrium with ions. Thus, equalling electrochemical potential of ions of the solute and the virtual bulk phase, we obtain two relations for the anions and the cations:

$$\mu_b^\pm = \mu^\pm = \pm F\phi + RT \ln(n^\pm) = \pm F\psi_b + RT \ln(n_b). \tag{8}$$

The difference between the electric potential ϕ and the bulk electric potential ψ_b introduces a third potential φ, which represents the electric measurement of the electrical distance between the point of the solution and its corresponding virtual bulk. This last electric potential can be identified as the consequence of the electrical double-layer effects. Indeed

Eq. (8) leads to the classical Boltzmann distributions of the ionic species (Israelachvili 1991):

$$n^{\pm} = n_b \exp(\mp\bar{\varphi}), \tag{9}$$

where the double-layer electric potential φ has been reduced as done before $\bar{\varphi} = F\varphi/RT$.

4.2 Virtual bulk pressure

A virtual bulk pressure p_b can be similarly defined using thermodynamical equilibrium of the solvent. Electric neutrality of water leads to the following equilibrium equation:

$$\frac{p}{\rho_l} + \frac{RT}{M_w}\ln\left(\frac{n^w}{n^w + n^+ + n^-}\right) = \frac{p_b}{\rho_l} + \frac{RT}{M_w}\ln\left(\frac{n_b^w}{n_b^w + 2n_b}\right), \tag{10}$$

where ρ_l is the mass density of the solution, n^w and n_b^w are the molar concentrations of water in the solution and in the virtual bulk, respectively, and M_w the volumic molar mass of water. As ionic concentrations can be neglected in comparison with solvent concentration, the mass density of the solution can be approximated by:

$$\rho_l \simeq n^w M_w \simeq n_b^w M_w. \tag{11}$$

Combining Eqs. (10) and (11), we have:

$$p_b = p - RT(n^- + n^+ - 2n_b). \tag{12}$$

According to Donnan (1924), the osmotic pressure defined by the van't Hoff relation $\pi = RT(n^- + n^+ - 2n_b)$ allows us to decompose hydraulic pressure in a bulk term and an osmotic one:

$$p_b = p - \pi. \tag{13}$$

4.3 Reformulation of the equations

Using the precedent change of variables, we can reformulate the problem in terms of bulk variables. The Poisson Eq. (1) written in term of reduced electric potential is changed thanks to Boltzmann distributions of ionic species (Eq. (9)) and becomes thus the classical Poisson–Boltzmann equation:

$$\Delta(\bar{\psi}_b + \bar{\varphi}) = \frac{1}{L_D^2}\sinh\,\bar{\varphi}, \tag{14}$$

where the Debye length characterizing the diffuse double-layer $L_D = \sqrt{\varepsilon\varepsilon_0 RT/2F^2 n_b}$ (Hunter 2001) is introduced.

To reformulate the Stokes Eq. (2), we first transform the gradient of hydraulic pressure using the decomposition (Eq. 13):

$$\nabla p = \nabla p_b + \nabla\pi. \tag{15}$$

The osmotic pressure gradient is then expressed by using the Boltzmann distributions of the ions (Eq. (9)) in the van't Hoff relation:

$$\nabla\pi = \nabla(2RTn_b(\cosh(\bar{\varphi}) - 1)) = 2RT(\cosh(\bar{\varphi}) - 1)\nabla n_b + 2RTn_b\sinh(\bar{\varphi})\nabla\bar{\varphi}. \tag{16}$$

Substituting Eqs. (15) and (16) in Stokes Eq. (2), recalling that $\bar{\phi} = \bar{\varphi} + \bar{\psi}_b$, we finally obtain the Stokes equation in terms of bulk variables:

$$\mu_f\Delta\mathbf{v} - \nabla p_b - 2RT(\cosh\,\bar{\varphi} - 1)\nabla n_b + 2RTn_b\sinh\,\bar{\varphi}\nabla\bar{\psi}_b = \mathbf{0}. \tag{17}$$

In this expression, we can clearly identify the three contributions for the fluid transport corresponding to gradients of: (1) virtual bulk pressure (hydraulic part, second term); (2) virtual bulk concentration (osmotic part, third term); (3) virtual bulk electric potential (electro-osmotic part, last term).

Considering the Boltzmann distributions of the ions Eq. (9), the chemical gradient of the Nernst–Planck Eq. (6) can be rewritten. The electric potential of the fluid is decomposed as before, and the new form of the Nernst–Planck equation is:

$$\frac{\partial(n_b\exp(\mp\bar{\varphi}))}{\partial t} + \nabla\cdot(n_b\exp(\mp\bar{\varphi})\mathbf{v}) = \nabla\cdot(D_{\pm}(\exp(\mp\bar{\varphi})(\nabla n_b \pm n_b\nabla\bar{\psi}_b))). \tag{18}$$

5 Upscaling procedure in the cylindric geometry

Since canaliculi and micropores ideally present the same cylindrical geometry, the upscaling procedure carried out is the same at these two levels of porosity. For this reason, this section only describes the general approach (homogenization) used to upscale the local description to the flow's scale. Specific results for each scale will be presented in the following part. One has to be careful: in this section, adjectives microscopic and macroscopic correspond to the local scale (pore scale) and the flow's scale, respectively. They do not correspond to the considered level of porosity. In what follows, the variables associated with the microscopic and macroscopic scales are designated respectively as fast and slow.

The goal is not here to repeat some results that are properly demonstrated elsewhere Moyne and Murad (2002a,b), but to show advantages of using bulk variables in this upscaling method. Readers interested in the homogenization method are invited to consult appropriate references, for instance, Sanchez-Palencia (1980), Hornung (1997) and Auriault (1991).

5.1 Use of periodic homogenization

In this framework, the medium is idealized as a bounded domain with a periodic structure. A microscopic characteristic length-scale l associated with the unit "cell" and a macroscopic length-scale L related to the overall dimensions of the medium are introduced. If the characteristic length l is very small in comparison with the macroscopic length L, we can introduce a small parameter ε defined by:

$$\varepsilon = \frac{l}{L} \ll 1. \tag{19}$$

One feature of the chosen geometry presented in Sect. 2 is that the macroscopic length L is in the order of magnitude of the longitudinal coordinate whereas the microscopic length l is related to the radial coordinate no matter what the considered scale is (microscale or mesoscale). For this configuration the scale separation assumption associated with Eq. (19) corresponds to a coordinate separation property too. Thus, we can define appropriate dimensionless variables:

$$z^* = \frac{z}{L}, \quad r^* = \frac{r}{l}. \tag{20}$$

All the functions h are then expanded in the form of an asymptotic development in terms of the perturbation parameter ε:

$$h(r^*, z^*) = \sum_{k=0}^{\infty} \varepsilon^k h_k(r^*, z^*). \tag{21}$$

An essential feature inherent to any upscaling technique is proper scaling of the dimensionless quantities that appear in the microscopic description. It is necessary to rewrite first the model at the microscale in dimensionless form before estimating the set of non-dimensional numbers, which characterize the local description. Moyne and Murad (2002a) propose such a discussion dealing with coefficients order of magnitude. Using scaling laws for coefficients proposed by these authors, the local mechanical model can be rewritten. Then, we are able to collect different terms with the same order of magnitude.

5.2 Slow and fast variables

Results of Moyne and Murad (2002a) lead to a distinction between slow variables, which are independent of the fast coordinate r, and fast variables, which may vary with r and z. In the fluid, slow variables are the bulk pressure p_b, the bulk concentration n_b and the bulk electric potential ψ_b. Fast variables are the fluid velocity $\mathbf{v}$ and the double-layer electric potential φ. Using these results in the considered geometry, different equations established in Sect. 4.3 can be simplified.

Poisson–Boltzmann Eq. (14) does not appear at the flow's scale and is transformed in:

$$\frac{\mathrm{d}^2\bar{\varphi}}{\mathrm{d}r^2} + \frac{1}{r}\frac{\mathrm{d}\bar{\varphi}}{\mathrm{d}r} = \frac{1}{L_D^2}\sinh\bar{\varphi}. \tag{22}$$

In the Debye–Hueckel approximation, that is to say if Debye length is small in comparison with pore scale (relevance of this approximation will be discussed in the next section), this equation can be linearized. After simplification by RT/F, this equation becomes:

$$\frac{\mathrm{d}^2\varphi}{\mathrm{d}r^2} + \frac{1}{r}\frac{\mathrm{d}\varphi}{\mathrm{d}r} = \frac{1}{L_D^2}\varphi. \tag{23}$$

Concerning the fluid movement in steady state, the velocity is longitudinal and only depends on the radial coordinate r:

$$\mathbf{v} = u(r)\mathbf{z}, \tag{24}$$

where $\mathbf{z}$ designates the unit vector of the longitudinal direction and $u(r)$ the component of the fluid velocity $\mathbf{v}$ along the $\mathbf{z}$-axis.

By introducing this relationship in Stokes Eq. (17), we obtain:

$$\mu_f\left(\frac{\mathrm{d}^2u}{\mathrm{d}r^2} - \frac{\mathrm{d}p_b}{\mathrm{d}z} + \frac{1}{r}\frac{\mathrm{d}u}{\mathrm{d}r}\right) - 2RT\,(\cosh\bar{\varphi} - 1)\,\frac{\mathrm{d}n_b}{\mathrm{d}z} + 2RTn_b\sinh\bar{\varphi}\frac{\mathrm{d}\bar{\psi}_b}{\mathrm{d}z} = 0. \tag{25}$$

Finally, Nernst–Planck Eq. (18) is modified in:

$$\frac{\partial(n_b\exp(\mp\bar{\varphi}))}{\partial t} + \frac{\partial(n_b\exp(\mp\bar{\varphi})u)}{\partial z} = \frac{\partial}{\partial z}\left(D_{\pm}\exp(\mp\bar{\varphi})\left(\frac{\partial n_b}{\partial z} \pm n_b\frac{\partial\bar{\psi}_b}{\partial z}\right)\right). \tag{26}$$

Thus, we have been able to rephrase the local description of the fluid at the flow's scale. Now we have to apply this physical description in both levels of porosity.

6 Solution at the two scales

The new upscaled description for the fluid obtained from the precedent change of variables is now written in the two levels of porosity. First, we intend to discuss Poisson–Boltzmann Eq. (22).

6.1 Discussion on the Poisson–Boltzmann equation

Solution of Poisson–Boltzmann Eq. (22) is necessary to evaluate the double-layer potential appearing in Stokes Eq. (25) that determines the fluid flow. For this reason, we have to find a solution for Nernst–Planck Eq. (26) at each scale.

If the reduced electrical double-layer potential remains small, the Debye–Hueckel approximation (Eq. (23)) is generally used (Hunter 2001). This case corresponds to large radii of the pores in comparison with Debye thickness (typically about a few nanometers). Since this approximation is no more efficient for small pores, semi-analytical approximations (Philip and Wooding 1970; Kang et al. 2002) or numerical computations are needed to obtain the potential distribution in cylindrical geometry from Poisson–Boltzmann Eq. (22). In the latter case, a finite volume scheme has been carried out to evaluate the double-layer potential.

Figure 2 illustrates the discrepancies between computational solutions of Poisson–Boltzmann Eq. (22) and closed-form analytic expressions obtained from Debye–Hueckel relation (Eq. (23)) for three values of the ratio of the pore radius to the Debye length. These profiles are plotted for a capillary pore with a radius R_P for an electrical potential of the solid wall of -3.55 mV (value of the zeta potential provided by Berreta and Pollack (1986)). When the double-layer thickness is small in comparison with the geometrical characteristic (see Fig. 2c for $R_P/L_D = 50$), the Debye–Hueckel approximation is good. However, as shown in Fig. 2a, 2b,

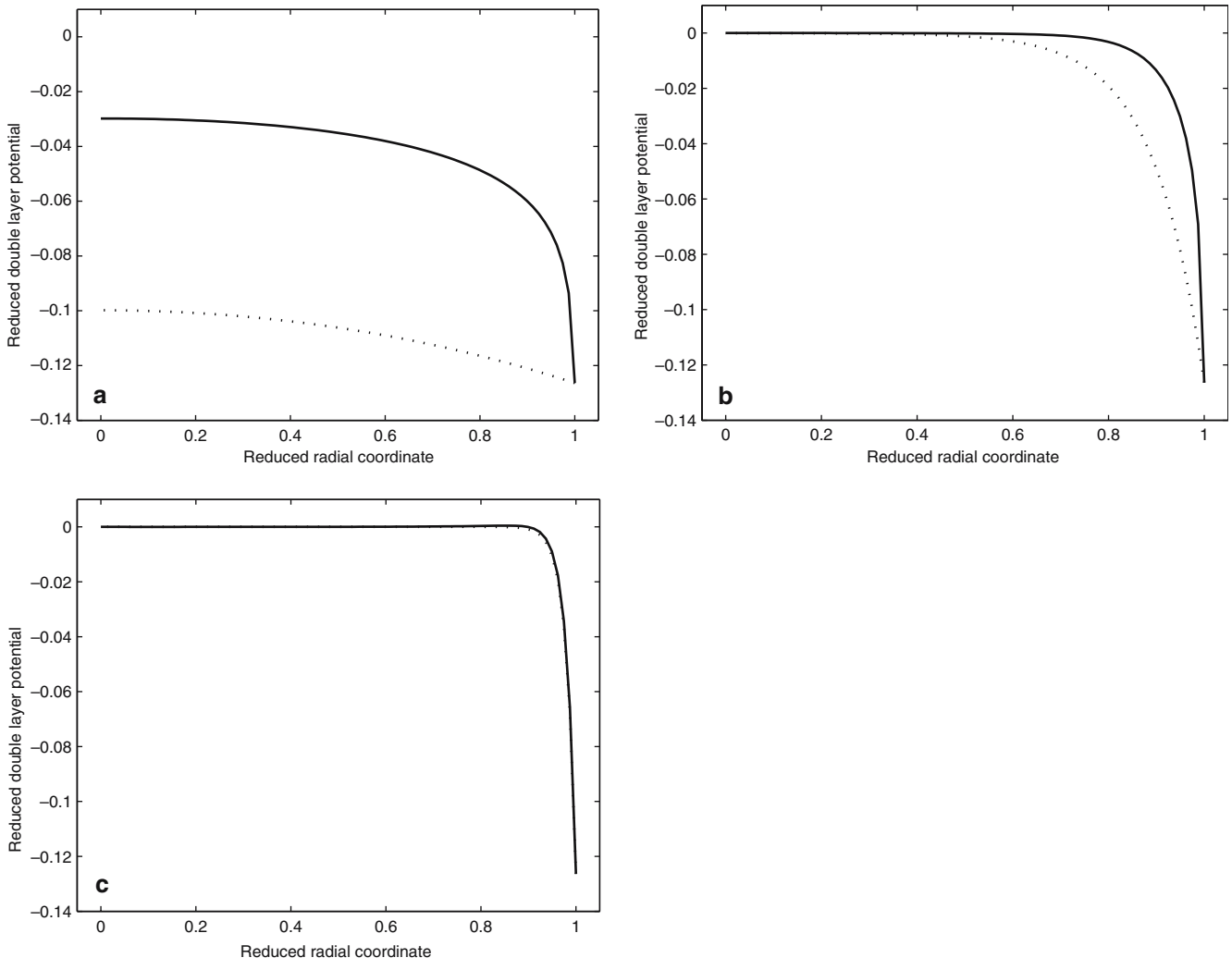

Fig. 2 Variations of $\bar{\varphi}$ versus r/R_P. Comparison of the computational solution of the Poisson–Boltzmann equation (*solid line*) with the Debye–Hueckel approximation (*dotted line*) in capillaries of different sizes: **a** $R_P = L_D$; **b** $R_P = 10L_D$; **c** $R_P = 50L_D$

this trend changes when the ratio R_P/L_D decreases. Then, the Debye–Hueckel approximation tends to overestimate the absolute value of the double-layer potential.

However, we need to work with geometrical lengths that are not too small to respect the continuum mechanics treatment of the problem. Curves obtained for a pore radius of the same order of magnitude as the Debye length are only illustrative. Indeed, nanometric dimensions corresponding to this case would need another method to analyse the fluid movement and would require another description of the physical behaviour of the electrolyte. For example, hydration forces, steric effects and Van der Walls forces cannot be neglected anymore at the molecular scale. In the present study, smallest pores are the intra-matrix ones. They are assumed to be large enough.

Annulus geometry of the mesoscale As numerical computations are rather time consuming, we prefer using the Debye–Hueckel approximation for large pores of the canaliculi. Thus the double-layer potential is analytically obtained from Eq. (23):

$$\varphi(r) = a_1 I_0\left(\frac{r}{L_D}\right) + a_2 K_0\left(\frac{r}{L_D}\right), \tag{27}$$

where I_n and K_n designate respectively the modified Bessel functions of the first and second kinds of order n; constants a_1 and a_2 are determined with the continuity condition of the electrical double-layer potential on the wall of the canaliculus ($r = R_C$) and the osteocyte process membrane ($r = R_M$). So we have at the mesoscale:

$$\varphi(r) = \frac{\varphi(R_C)(I_0(\frac{r}{L_D})K_0(\frac{R_M}{L_D}) - I_0(\frac{R_M}{L_D})K_0(\frac{r}{L_D})) + \varphi(R_M)(I_0(\frac{R_C}{L_D})K_0(\frac{r}{L_D}) - I_0(\frac{r}{L_D})K_0(\frac{R_C}{L_D}))}{I_0(\frac{R_C}{L_D})K_0(\frac{R_M}{L_D}) - I_0(\frac{R_M}{L_D})K_0(\frac{R_C}{L_D})}. \tag{28}$$

The radial coordinate r here refers to the canaliculus radius (mesoscale).

Cylindrical geometry of the micropores In the small pores of the collagen-apatite matrix, which are assumed to be capillaries, a finite volume scheme has to be implemented to evaluate the double-layer potential variation with the microscopic radial coordinate. Corresponding boundary conditions are given by the axisymetric property of the problem and Dirichlet condition on the pore's wall.

6.2 Modified Darcy law

Since we know the double-layer potential in each level of porosity, solution of Stokes Eq. (25) describes the fluid flow. In this equation, three driving mechanisms for fluid flow are clearly distinguished. The first two terms are characteristics of a Poiseuille flow. The next term, where the chemical gradient appears, corresponds to the osmotic part of the whole fluid movement. Finally, the term with electric gradient is identified as the electro-osmotic flow. If Stoke's equation presents the same form when it is written in the mesopores or the micropores, we insist on the fact that the different coordinates (radial or longitudinal) refer to each structural level and should not be confused.

6.2.1 Poiseuille velocity

Using linearity of the problem, the velocity u is decomposed into three parts resulting from each precedingly mentioned effect:

$$u = u_P + u_C + u_E. \tag{29}$$

At each scale, the Poiseuille velocity u_P is the solution of the following equation:

$$-\frac{\mathrm{d}p_b}{\mathrm{d}z} + \mu_f \left(\frac{\mathrm{d}^2 u_P}{\mathrm{d}r^2} + \frac{1}{r}\frac{\mathrm{d}u_P}{\mathrm{d}r} \right) = 0. \tag{30}$$

Moreover, no-slip conditions on boundary walls are assumed.

At each pore scale, it is possible to average each velocity profile on the corresponding transverse cross-section S leading to:

$$< u_P >= \frac{1}{S}\int_S u_P \mathrm{d}S = -K_P \frac{\mathrm{d}p_b}{\mathrm{d}z}, \tag{31}$$

where $K_P = k_P/\mu_f$ is the Poiseuille permeability (k_P is the intrinsic permeability of Poiseuille). As a consequence, the Poiseuille permeability is a parameter depending only on the pore geometry and the fluid viscosity.

Annulus geometry of the mesoscale For this geometry and this scale, the non-slip conditions ($u_P[R_M] = u_P[R_C] = 0$) lead to:

$$u_P(r) = \frac{r^2 \ln\left(\frac{R_M}{R_C}\right) + R_M^2 \ln\left(\frac{R_C}{r}\right) + R_C^2 \ln\left(\frac{r}{R_M}\right)}{4\mu_f \ln\left(\frac{R_C}{R_M}\right)} \frac{\mathrm{d}p_b}{\mathrm{d}z}, \tag{32}$$

where R_C and R_M are the canaliculus and the osteocyte process radius, respectively.

Using relation (31) with $S = \pi(R_C^2 - R_M^2)$, the Poiseuille permeability K_P in the mesopores is obtained as:

$$K_P = \frac{1}{8} \frac{R_C^2 \left(\ln\left(\frac{R_C}{R_M}\right) - 1 \right) + R_M^2 \left(\ln\left(\frac{R_C}{R_M}\right) + 1 \right)}{\mu_f \ln\left(\frac{R_C}{R_M}\right)}, \tag{33}$$

Cylindrical geometry of the micropores For this geometry and this scale, assuming a non-slip condition leads to a classically parabolic velocity profile:

$$u_P(r) = -\frac{R_m^2}{4\mu_f}\left[1 - \frac{r^2}{R_m^2}\right]\frac{\mathrm{d}p_b}{\mathrm{d}z}, \tag{34}$$

where R_m is the micropore radius.

Using relation (31) with $S = \pi R_m^2$, the Poiseuille permeability K_P in the microporosity is obtained as:

$$K_P = \frac{R_m^2}{8\mu_f}. \tag{35}$$

6.2.2 Electro-osmotic velocity

In an analogous way, the electro-osmotic flow is the solution of:

$$2RTn_b \sinh\bar{\varphi}\frac{\mathrm{d}\bar{\psi}_b}{\mathrm{d}z} + \mu_f\left(\frac{\mathrm{d}^2 u_E}{\mathrm{d}r^2} + \frac{1}{r}\frac{\mathrm{d}u_E}{\mathrm{d}r}\right) = 0. \tag{36}$$

Using Poisson–Boltzmann Eq. (22), the term with the hyperbolic sine function can be replaced by the Laplace operator applied to the double-layer electrical potential:

$$\frac{\mathrm{d}^2 g}{\mathrm{d}r^2} + \frac{1}{r}\frac{\mathrm{d}g}{\mathrm{d}r} = 0,$$
$$\text{where } g(r) = 2RTn_b L_D^2 \frac{\mathrm{d}\bar{\psi}_b}{\mathrm{d}z}\bar{\varphi}(r) + \mu_f u_E(r). \tag{37}$$

This last equation allows us to express analytically the function $g(r)$.

As done before, the two electro-osmotic profiles can be averaged on the corresponding transverse section, in order to give an expression of the electro-osmotic permeability K_E for each level of porosity:

$$< u_E >= \frac{1}{S}\int_S u_E \mathrm{d}S = -K_E \frac{\mathrm{d}\bar{\psi}_b}{\mathrm{d}z}. \tag{38}$$

As a consequence, this parameter quantifies electro-osmotic part of the transport and depends on pores geometry, electrical conditions on their walls and Debye length.

Annulus geometry of the mesoscale At the mesoscale, a closed-form analytic solution of the electric double-layer potential is obtained using the Debye–Hueckel approximation. Using non-slip conditions at the osteocyte process and the canaliculus wall ($u_E[R_M] = u_E[R_C] = 0$), the electro-osmotic velocity in the canaliculus is deduced.

Thanks to the Debye–Hueckel approximation, an analytic expression of the permeability defined from Eq. (38) can be provided at the mesoscale:

$$
\begin{aligned}
K_E = &-\frac{RTn_bL_D^2}{\mu_f \ln(\frac{R_M}{R_C})(R_M^2-R_C^2)(I_0(\frac{R_C}{L_D})K_0(\frac{R_M}{L_D})-I_0(\frac{R_M}{L_D})K_0(\frac{R_C}{L_D}))}\\
&\times\Bigg[\bar{\varphi}(R_C)R_C^2((1+2\ln(\frac{R_M}{R_C}))I_0(\frac{R_C}{L_D})K_0(\frac{R_M}{L_D})\\
&+(-1+2\ln(\frac{R_C}{R_M}))I_0(\frac{R_M}{L_D})K_0(\frac{R_C}{L_D}))\\
&+\bar{\varphi}(R_M)R_M^2((1+2\ln(\frac{R_C}{R_M}))I_0(\frac{R_C}{L_D})K_0(\frac{R_M}{L_D})\\
&+(-1+2\ln(\frac{R_M}{R_C}))I_0(\frac{R_M}{L_D})K_0(\frac{R_C}{L_D}))\\
&+\bar{\varphi}(R_C)R_M^2(-I_0(\frac{R_C}{L_D})K_0(\frac{R_M}{L_D})+I_0(\frac{R_M}{L_D})K_0(\frac{R_C}{L_D}))\\
&+\bar{\varphi}(R_M)R_C^2(-I_0(\frac{R_C}{L_D})K_0(\frac{R_M}{L_D})+I_0(\frac{R_M}{L_D})K_0(\frac{R_C}{L_D}))\\
&+4\bar{\varphi}(R_C)R_CL_D(I_1(\frac{R_C}{L_D})K_0(\frac{R_M}{L_D})\ln(\frac{R_C}{R_M})\\
&+I_0(\frac{R_M}{L_D})K_1(\frac{R_C}{L_D})\ln(\frac{R_C}{R_M}))\\
&+4\bar{\varphi}(R_M)R_ML_D(I_1(\frac{R_M}{L_D})K_0(\frac{R_C}{L_D})\ln(\frac{R_C}{R_M})\\
&+I_0(\frac{R_C}{L_D})K_1(\frac{R_M}{L_D})\ln(\frac{R_C}{R_M}))\\
&+4\bar{\varphi}(R_C)R_ML_D(I_1(\frac{R_M}{L_D})K_0(\frac{R_M}{L_D})\ln(\frac{R_M}{R_C})\\
&+I_0(\frac{R_M}{L_D})K_1(\frac{R_M}{L_D})\ln(\frac{R_M}{R_C}))\\
&+4\bar{\varphi}(R_M)R_CL_D(I_1(\frac{R_C}{L_D})K_0(\frac{R_C}{L_D})\ln(\frac{R_M}{R_C})\\
&+I_0(\frac{R_C}{L_D})K_1(\frac{R_C}{L_D})\ln(\frac{R_M}{R_C}))\Bigg].
\end{aligned}
\tag{39}
$$

Cylindrical geometry of the micropores At the microscale, non-slip ($u_E[R_C]=0$) and symmetry conditions associated with the numerically evaluated double-layer potential helps us to obtain a closed-form solution of electro-osmotic velocity in the micropores.

Unfortunately, an analytical solution for the electro-osmotic microscale permeability cannot be provided since there is no a closed-form analytic solution of the double-layer potential in the micropores.

6.2.3 Osmotic velocity

To complete this study, the problem of osmotic flow is written at each scale:

$$
-2RT(\cosh\bar{\varphi}-1)\frac{\mathrm{d}n_b}{\mathrm{d}z}+\mu_f\left(\frac{\mathrm{d}^2u_C}{\mathrm{d}r^2}+\frac{1}{r}\frac{\mathrm{d}u_C}{\mathrm{d}r}\right)=0. \tag{40}
$$

Knowing the electrical double-layer potential, this equation is numerically solved in the mesopores and in the micropores.

Resulting osmotic velocity profiles can be averaged on the transverse section to obtain two equations introducing osmotic permeability K_C:

$$
<u_C>=\frac{1}{S}\int_S u_C\mathrm{d}S=-K_C\frac{\mathrm{d}n_b}{\mathrm{d}z}. \tag{41}
$$

Finally, using a parallel resolution of the Stoke's problem, we have been able to describe the averaged fluid flow in the canaliculi (mesopores) and in the micropores inside the collagen-apatite matrix with two independent modified Darcy laws of the form:

$$
\begin{aligned}
<u> &= <u_P> + <u_E> + <u_C>\\
&= -K_P\frac{\mathrm{d}p_b}{\mathrm{d}z}-K_E\frac{\mathrm{d}\bar{\psi}_b}{\mathrm{d}z}-K_C\frac{\mathrm{d}n_b}{\mathrm{d}z}.
\end{aligned}
\tag{42}
$$

Different permeabilities have to be evaluated at each scale. It will then be possible to quantify the contribution of hydraulic, electro-osmotic and osmotic effect on fluid flow at each level of porosity.

7 Results and discussion

For the two levels of porosity that are of interest in this study, a modified Darcy law (42) has been proposed to describe the fluid movement. Advantage of these laws is that it allows us to estimate the role of the three driving effects governing the interstitial fluid movement at the canaliculus scale and inside the solid matrix.

For all presented results, the virtual bulk concentration is fixed to 0.01 mol/l. The electrolyte is characterized by its relative permeability of 75.34 (Cowin et al. 1995) and its viscosity of 0.65 cPo (0.65×10^{-3} Pl).

At each level of porosity, the corresponding modified Darcy law (Eq. (42)) is used to determine the magnitude of Poiseuille, electro-osmosis and chemo-osmosis effects on the fluid flow.

7.1 Study at the mesoscale: fluid movement in the canaliculi

In this section, we intend to study the electrolyte movement in the canaliculus. To achieve this objective, it is necessary to choose suitable orders of magnitude of hydraulic, electrical and chemical variations at the flow scale. This scale corresponds to the flow distance, that is to say the osteon radius $\delta z = 160\ \mu$m (Piekarski and Munro 1977), where δ designates the magnitude of variation of the variable. Concerning the hydraulic gradient, bibliographic references treat it in terms of hydraulic pressure whereas the hydraulic gradient appearing in the modified Darcy law (Eq. (42)) of the present model corresponds to the virtual bulk pressure. We have to first check that the Donnan osmotic pressure introduced by Eq. (13) can indeed be neglected. For concentrations physiologically observed (between 0.01 and 0.5 mol/l), osmotic pressure is such that $\pi\sim0.1$ bar (10^4 Pa). As a consequence, the pressure decomposition (Eq. (13)) reduces to $p=p_b$ if

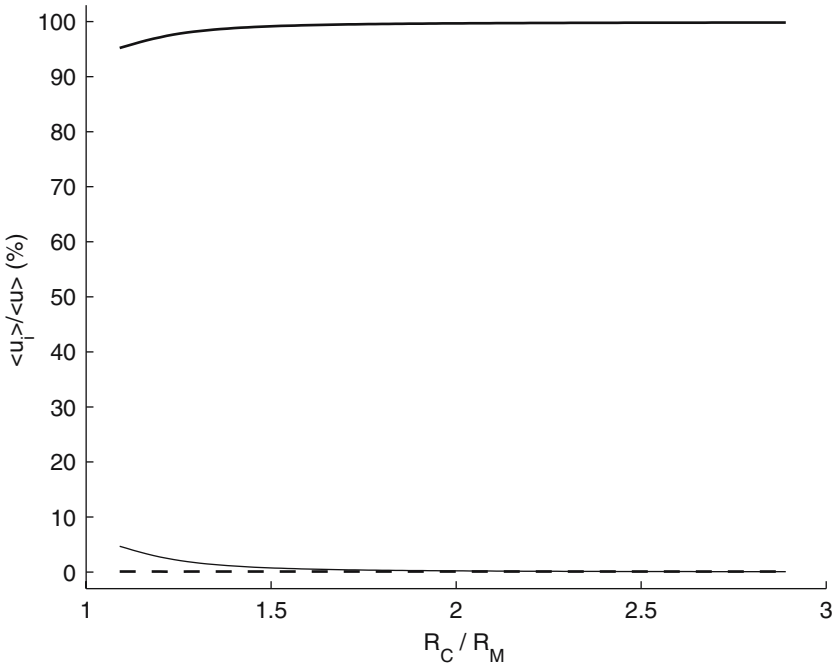

Fig. 3 Variations of $< u_i > / < u >$ versus R_C/R_M, where $< u_i >$ designates $< u_P >$ (*thick line*), $< u_E >$ (*thin line*) or $< u_C >$ (*dashed line*). Comparison between Poiseuille, electro-osmosis and osmosis effects driving the fluid in the mesopores for various geometrical characteristics

hydraulic pressure is greater than a thousands of pascals. By referring to precedent studies dealing with the fluid movement within the canaliculi, pressure variations are not well described, and are often estimated from a flow modelling. Recently Gururaja et al. (2005) showed that fluid pressures depend on both the magnitude of the loading applied to the bone, and the cyclic frenquency of such loading. If Wang et al. 2003 worked with pressures about 0.1 bar (10^4 Pa) (typically corresponding to the blood pressure), Piekarski and Munro (1977) identified pressure variations of about 1 bar, which remains small in comparison with values of several bars from Zhang et al. (1998). On the other hand, streaming potential variations are estimated with respect to measurements with micro-electrodes of Starkenbaum et al. (1979): $\delta\bar{\psi}_b = (F/RT)\delta\psi_b = (F/RT) \times 0.002$ V. Moreover chemical variations for the flow's scale are taken to be 0.01 mol/l.

Use of Eqs. (31), (38) and (41) provide the order of magnitude of the Poiseuille effect ($|< u_P >| = K_P[\delta p_b/\delta z]$), electro-osmosis effect ($|< u_E >| = K_E[\delta\bar{\psi}_b/\delta z]$) and chemo-osmosis effect ($|< u_C >| = K_C[\delta n_b/\delta z]$).

Sensitivity of the geometry In a first approach, influence of the geometry is studied with an electrical potential of canaliculus walls fixed at −3.55 mV from Berreta and Pollack (1986).

Figure 3 presents for a given radius of the osteocyte ($R_M = 55$ nm) the evolution of the three parts of the flow with an increasing ratio $\bar{R}_C = R_C/R_M$ with the bulk pressure variations of Wang et al. (2003). If the osmotic effect remains always almost zero, electro-osmotic flow is a few percent for small annular spaces. But it soon becomes not significant as the ratio $\bar{R}_C = R_C/R_M$ reaches 1.5. Considering a small value of the double-layer electrical potential in the frame of Debye–Hueckel approximation, the hyperbolic cosine appearing in the osmotic Eq. (40) is developed into a series. Only a second-order term is kept. As a consequence, the resulting osmotic flow is weak. On the other hand, the hyperbolic sine function of electro-osmotic Eq. (36) appears as a first-order term. This explains why even though the osmotic term can be neglected at the mesoscale, the electro-osmotic effect may have a little influence on fluid flow.

Figure 3 seems indeed to indicate that Poiseuille effect is the most important driving force at the mesoscale. Indeed the Poiseuille permeability only depends on the pore size and for classically observed canaliculi radii (You et al. 2004), this parameter is the major one when compared with osmotic and electro-osmotic ones.

Aim of Fig. 4 is to confirm this trend with various hydraulic gradients and two sets of wall electric potential (−3.55 and −20 mV). For this figure, osmosis has been neglected. Two cases are studied for a fixed geometry ($R_M = 50$ nm): (1) $\bar{R}_C = 1.5$; and (2) $\bar{R}_C = 2.5$. This second case corresponds to averaged sizes of the osteocyte process and the canaliculus as observed by You et al. (2004). Curves of this figure conform to those presented in Fig. 3. Indeed electro-osmosis effect remains weak when the reduced radius of the canaliculus becomes large. Increase in electro-osmotic effect with increase of wall electrical potential or decrease in hydraulic gradient is observed, but this phenomenon remains insignificant.

Considering these results at the mesoscale, the Poiseuille effect seems to be the most important driving effect in fluid movement. As a consequence, use of classical Darcy law is sufficient to describe fluid flow within the canaliculi.

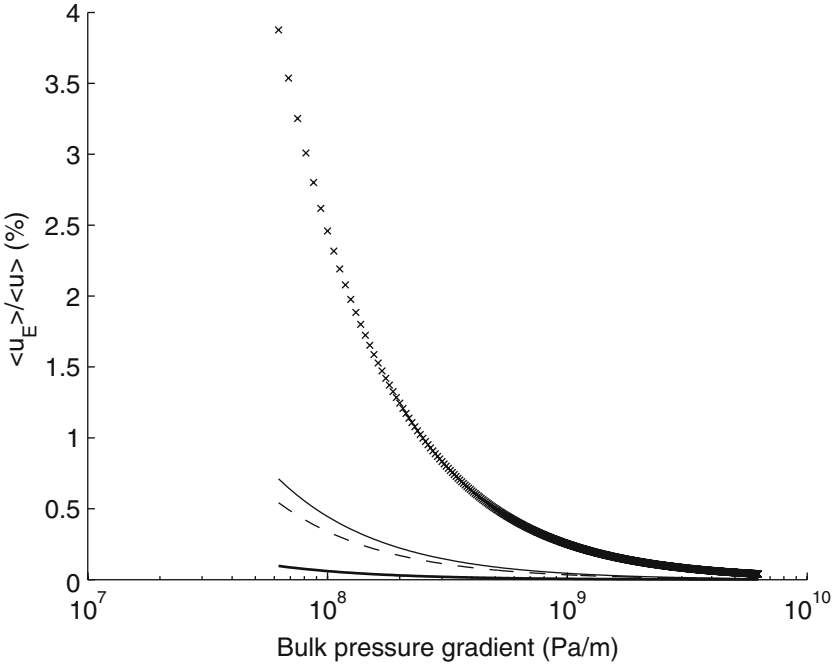

Fig. 4 Effects of hydraulical and electrical conditions in two geometrical cases: (1) when $\bar{R}_C = 1.5$, considering a boundary electrical potential of -3.55 mV (*thin line*), and of -20 mV (*cross sign*); (2) when $\bar{R}_C = 2.5$, considering a boundary electrical potential of -3.55 mV (*thick line*) and of -20 mV (*dashed line*)

Influence of the presence of microfibers Before studying what happens at the microscale, we discuss microfibres presence in the annulus space between canaliculus and osteocyte cell process. Presence of such microelements have been taken into account in the model of Cowin et al. (1995) and observed by You et al. (2004) 9 years later. Geometrical organization of these microfibres is described by their radius R_F (0.6 nm for Cowin et al. (1995) and 3.65 nm for You et al. (2004)) and the inter-fibers space d_F (7 nm for Cowin et al. (1995) and 25 nm for You et al. (2004)). Using the flow model of Tsay and Weinbaum (1991) and Weinbaum et al. (1994), Cowin et al. (1995) were able to obtain lower Poiseuille permeabilities than those calculated here. Consequently, taking into account the presence of such microfibers could slightly change the comparison between electro-osmotic and hydraulic effects. For this reason, it is necessary to analyse the influence of presence of microfibers. That is the purpose of Fig. 5. In this figure, the ratio between the Poiseuille flow calculated with the Cowin et al. (1995) approach and the same flow calculated in the present model without microfibres is plotted versus the reduced canaliculus radius for two values of the osteocyte process under consideration.

Introduction of microfibres results in a smaller Poiseuille flow. However, this decrease remains very weak considering the geometrical characteristics of You et al. (2004). Indeed, fibres density is not sufficient to significantly disturb Poiseuille flow. Concerning the fibrous net modelled by Cowin et al. (1995), it generates a remarkable decrease of the Poiseuille effect for large values of the reduced radius of the canaliculus $\bar{R}_C$. Nevertheless, such changes of the Poiseuille permeability are not strong enough to radically modify results shown by the two precedent figures. Indeed, the most favourable situation for having a lower Poiseuille effect because of the microfibres (high values of $\bar{R}_C$) corresponds to the worst configuration for having an important electro-osmotic effect, and vice versa, the less favourable situation for having a lower Poiseuille effect as the microfibres (small values of $\bar{R}_C$) correspond to the best configuration for having an important electro-osmotic effect.

7.2 Study at the microscale: fluid movement inside the collagen-apatite matrix

In this section, a similar approach is conducted to study fluid flow within micropores inside the collagen-apatite matrix. As said in Sect. 2, which deals with geometrical configuration, the size of these pores is not well known. According to measurements of Holmes et al. 1953, the radius of the micropores R_m varies between 5 and 12.5 nm. We assume that they present a capillary geometry. The length of the micropores is not known, but it is assumed to be large in comparison with their radius, so that the scaling separation property given by Eq. (19) can be verified to apply the same modelling procedure. Electrical potential of the micropores walls and different physical variations at the flow scale are assumed to be the same as those used in Sect. 7.1. Since the length of the flow scale, which corresponds to the longitudinal length of the micropores, is not explicitly given, the three driving gradients are expressed as a variation along this length.

Results are presented in three figures showing the different parts of fluid flow for: (1) a small value of the wall's

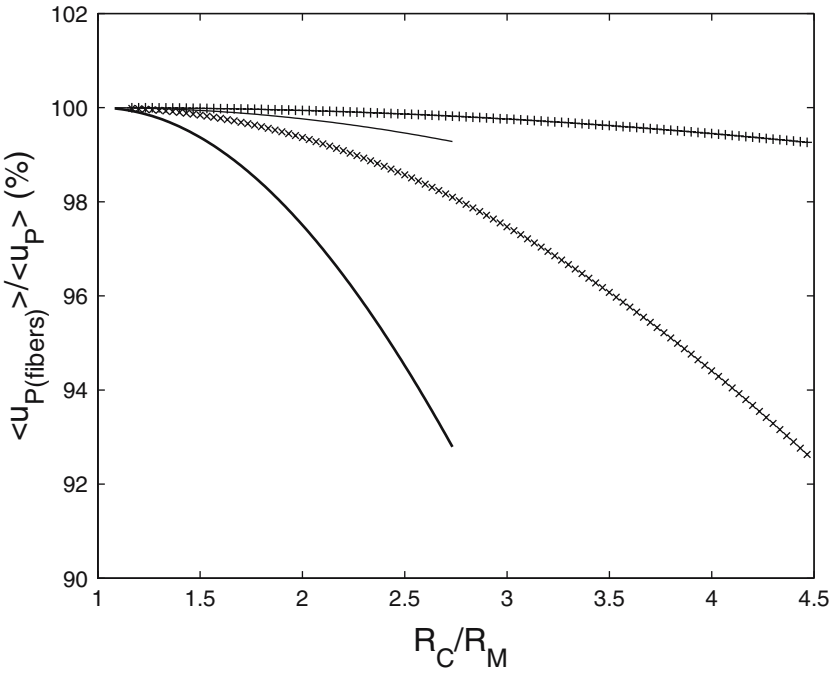

Fig. 5 Poiseuille effect considering or not fibers for different geometrical values: case of Cowin et al. (1995) ($R_F = 0.6$ nm and $d_F = 7$ nm) for $R_M = 30$ nm (*cross sign*) and $R_M = 60$ nm (*thick line*) case of You et al. (2004) ($R_F = 3.65$ nm and $d_F = 25$ nm) for $R_M = 30$ nm (*plus sign*) and $R_M = 60$ nm (*thin line*)

electrical potential (-3.55 mV) and hydraulic variations corresponding to blood's pressure data of Wang et al. (2003), Fig. 6a); (2) a high value of the wall's electrical potential (-20 mV) and hydraulic variations corresponding to blood pressure's order of magnitude (Fig. 6b); and (3) a high value of the wall's electrical potential (-20 mV) and hydraulic variations about 1 bar (10^5 Pa, Fig. 6c). For each of these figures, influence of micropore radius R_m is analysed.

Concerning Fig. 6a, if hydraulic effect is still the most important part, influence of electro-osmosis and osmosis cannot be neglected as the micropore's radius decreases. Nevertheless, this trend would not be noticeable for higher values of hydraulic gradients. In Fig. 6b, 6c, role of the wall's potential is emphasized. Indeed, for higher values of this parameter, electro-osmotic and osmotic effects are close to the hydraulic effect corresponding to blood pressure variations, and they cannot be neglected for small micropores, even for higher hydraulic gradients.

Thus, our results seem to indicate that, contrary to observations at the mesoscale, coupled phenomena are not insignificant in the micropores. The smaller are the pores or the highest are the wall's potentials, the most necessary it is to include electro-osmosis and osmosis effects in the description of fluid flow.

7.3 Limitations of the study

The present study puts into light the important role of the electro-chemical effects at the microscale. Furthermore, it is necessary to include phenomena occurring in the microstructure to describe more accurately the fluid movement within bone at the macroscopic scale. Fluid flow can also depend on other factors, such as ageing, hormonal expressions or physical exercices. For instance, influence of ageing can be accounted for through variations of the microstructure, the mineral content of the bone matrix and the dimensions of pores. However, biochemical variations are not modelled but could be introduced through new boundary conditions and exchanges between porosity levels. For example, the role of the Haversian system concerning interstitial fluid influx could be integrated in the boundary conditions as explained in Sect. 2. Adding mass exchange terms between the different porosity levels could be a significant amelioration of this model. A suitable description of neural, hormonal and metabolic influences could complete the proposed model to better describe bone fluid flow.

8 Conclusion

A multiscale modelling of the osteon has been proposed to analyse hydro-electro-chemical couplings governing fluid movement within the bone. This modelling is derived for a cylindrical geometry with circular cross-section using a change of variables resulting from the introduction of a virtual bulk solution. Two levels of porosity have been studied: the mesopores of the canaliculi and the micropores inside the collagen-apatite matrix. At the mesoscale, fluid movement is caused essentially by the hydraulic gradient, even if fibers are present in the canalicular spaces. As a consequence,

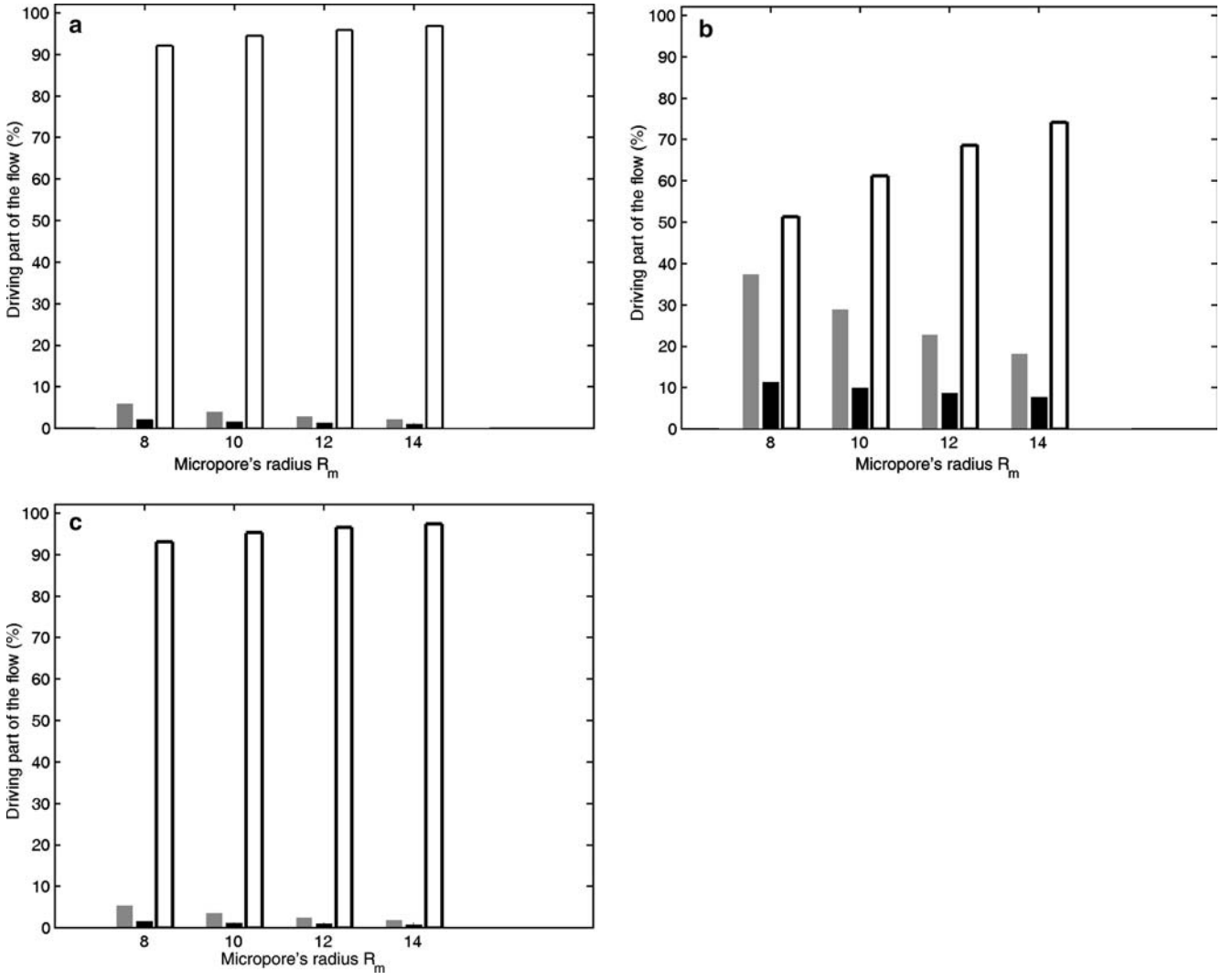

Fig. 6 Comparison between the three driving effects in the microporosity (electro-osmosis in grey, osmosis in black and Poiseuille effect in white): **a** for a low wall's potential of -3.55 mV and pressure variations of 0.08 bar (8×10^3 Pa); **b** for a high wall's potential of -20 mV and pressure variations of 0.08 bar (8×10^3 Pa); **c** for a high wall's potential of -20 mV and pressure variations of 1 bar (10^5 Pa)

classical Darcy law is suitable to describe interstitial fluid velocity through the mesopores. However, this law becomes less efficient in these phenomena description at the microscale.

In its first form, this work is a good tool to understand the role of each scale in the multiphysical transport of fluid movement. It will also be useful to include in the model the biochemical effects. At this stage, these results are still somewhat qualitative, but they provide a new way to analyse osteon's mechanical response.

References

Arramon Y, Nauman E (2001) The intrinsic permeability of cancellous bone. In: Cowin S (ed) Bone mechanics handbook, chap 5, 2nd edn. CRC, Boca Raton, FL, pp 1–17

Auriault J-L (1991) Heterogeneous medium. Is an equivalent macroscopic description possible? Int J Eng Sci 29:785–795

Basset C, Becker R (1962) Generation of electrical potentials by bone in response to mechanical stress. Science 137:1063–1064

Berreta D, Pollack S (1986) Ion concentration effects on the zeta potential of bone. J orthop Res 4:337–341

Biot M (1941) General theory of three-dimensional consolidation. J Appl Phys 12(2):155–164

Buckwalter J, Glimcher M, Cooper R, Recker R (1995) Bone biology. Part i: Structure, blood supply, cells, matrix, and mineralization. J Bone Joint Surg Am 77:1256–1275

Cowin S (2001) Bone poroelasticity. In: Cowin S (ed) Bone mechanics handbook, chap 23, 2nd edn. CRC, Boca Raton, FL, pp 1–31

Cowin S (2002) Mechanosensation and fluid transport in living bone. J Musculoskel Neuron Interaction 2(3):256–260

Cowin S, Weinbaum S, Zeng Y (1995) A case for bone canaliculi as the anatomical site of strain generated potentials. J Biomech 28(11):1281–1297

Donnan F (1924) The theory of membrane equilibrium. Chem Rev 1:73–90

Dormieux L, Barboux P, Coussy O, Dangla P (1995) A macroscopic model of the swelling phenomenon of a saturated clay. Eur J Mech A/Solids 14(6):981–1004

Gu W, Lai W, Mow V (1998) A mixture theory for charged-hydrated soft tissues containing multi-electrolytes : passive transport and swelling behaviors. J Biomech Eng 120:169–180

Gururaja S, Kim H, Swan C, Brand R, Lakes R (2005) Modeling deformation-induced fluid flow in cortical bone's canalicular-lacunar system. Ann Biomed Eng 33:7–25

Holmes J, Davies D, Meath W, Beebe RA (1953) Gas adsorption and surface structure of bone mineral. Biochemistry 3:2019–2024

Hornung U (1997) Homogenization and porous media. Springer, Berlin Heidelberg New York

Hunter R (1981) Zeta potential in colloid science: principles and applications. Academic, New York

Hunter R (2001) Foundations of colloid science. Oxford University Press, New York

Israelachvili J (1991) Intermolecular and surface forces. Academic, New-York

Kang Y, Yang C, Huang X (2002) Electroosmotic flow in a capillary annulus with high zeta potentials. J Colloid Interf Sci 253:285–294

Kim Y, Kim J, Kim Y, Rho J (2002) Effects of organic matrix proteins on the interfacial structure at the bone-biocompatible nacre interface in vitro. Biomaterials 23:2089–2096

Landau L, Lifshitz E (1960) Electrodynamics of continuous media. Pergamon Press, Oxford

Lemaire T (2004) Couplages Électro-chimio-hydro-mécaniques dans les milieux argileux. PhD thesis, Institut National Polytechnique de Lorraine, Nancy

Lemaire T, Moyne C, Stemmelen D, Murad M (2002) Electro-chemo-mechanical couplings in swelling clays derived by homogenization : electroviscous effects and onsager's relations. In: Auriault J, Geindreau C, Royer P, Bloch J-F, Boutin C, Lewandowska J (eds) Poromechanics II, proceedings of the second Biot conference on poromechanics, Grenoble, France. Balkema Publishers, Lisse, pp 489–500

Lyklema J (1995) Foundamentals of interface and colloid science. Academic, London

Mak A, Zhang J (2001) Numerical simulation of streaming potentials due to deformation-induced hierarchical flows in cortical bone. J Biomech Eng 123(1):66–70

Moyne C, Murad M (2002a) Electro-chemo-mechanical couplings in swelling clays derived from a micro/macro-homogenization procedure. Int J Solids and Structures 39(25):6159–6190

Moyne C, Murad M (2002b) Macroscopic behavior of swelling porous media derived from micromechanical analysis. Transport Porous Med 50:127–151

Philip J, Wooding R (1970) Solution of the poisson-boltzmann equation about a cylindrical particle. J Chem Phys 52:953–959

Piekarski K, Munro M (1977) Transport mechanism operating between blood supply and osteocytes in long bones. Nature 269(5623): 80–82

Pollack S (2001) Streaming potentials in bone. In: Cowin S (ed) Bone mechanics handbook, Chap 24, 2nd edition. CRC, Boca Raton, FL, pp 1–22

Pollack S, Petrov N, Salzstein R, Brankov G, Blagoeva R (1984) An anatomical model for streaming potentials in osteons. J Biomech 17:627–636

Rémond A, Naili S (2004) Cyclic loading of a transverse isotropic poroelastic cylinder: a model for the osteon. C R Mec 332(9):759–766

Samson E, Marchand J, Robert J-L, Bournazel J-P (1999) Modelling ion diffusion mechanisms in porous media. Int J Numer Meth Eng 46:2043–2060

Sanchez-Palencia, E (1980) Non-homogenous media and vibration theory, In: Lectures notes in Physics, vol 127. Springer, Berlin Heidelberg New York

Sasidhar V, Ruckenstein E (1981) Electrolyte osmosis through capillaries. J Colloid Interf Sci 8:439–457

Starkenbaum W, Pollack S, Korostoff E (1979) Microelectrode studies of stress generated potentials in four point bending of bone. J Biomed Mater Res 13:729–751

Tsay R, Weinbaum S (1991) Viscous flow in a channel with periodic cross-bridging fibers: exact solutions and brinkman approximation. J Fluid Mech 226:125–148

Wang L, Fritton SP, Weinbaum S, Cowin S (2003) On bone adaptation due to venous stasis. J Biomech 36(10):1439–1451

Weinbaum S, Cowin S, Zeng Y (1994) A model for the excitation of osteocytes by mechanical loading-induced bone fluid shear stresses. J Biomech 27(3):339–360

Yasuda I (1964) Piezoelectricity of living bone. J Kyoto Pref Med 53:2019–2024

You L, Weinbaum S, Cowin S, Schaffler M (2004) Ultrastructure of the osteocyte process and its pericellular matrix. Anat Rec 278A(2):505–513

Zhang D, Weinbaum S, Cowin S (1998) On the calculation of bone pore water pressure due to mechanical loading. Int J Solids and Structures 35(34-35):4981–4997